ARTICLES
https://doi.org/10.1038/s41566-021-00761-7

nature photonics

Check for updates

Hertz-linewidth semiconductor lasers using CMOS-ready ultra-high-*Q* microresonators

Warren Jin[1,4], Qi-Fan Yang[2,4], Lin Chang[1,4], Boqiang Shen[2,4], Heming Wang[2,4], Mark A. Leal[1], Lue Wu[2], Maodong Gao[2], Avi Feshali[3], Mario Paniccia[3], Kerry J. Vahala[2]✉ and John E. Bowers[1]✉

Driven by narrow-linewidth bench-top lasers, coherent optical systems spanning optical communications, metrology and sensing provide unrivalled performance. To transfer these capabilities from the laboratory to the real world, a key missing ingredient is a mass-produced integrated laser with superior coherence. Here, we bridge conventional semiconductor lasers and coherent optical systems using CMOS-foundry-fabricated microresonators with a high *Q* factor of over 260 million and finesse over 42,000. A five-orders-of-magnitude noise reduction in the pump laser is demonstrated, enabling a frequency noise of 0.2 Hz² Hz⁻¹ to be achieved in an electrically pumped integrated laser, with a corresponding short-term linewidth of 1.2 Hz. Moreover, the same configuration is shown to relieve the dispersion requirements for microcomb generation that have handicapped certain nonlinear platforms. The simultaneous realization of this high *Q* factor, highly coherent lasers and frequency combs using foundry-based technologies paves the way for volume manufacturing of a wide range of coherent optical systems.

The benefits of high-coherence lasers extend to many applications. Hertz-level linewidths are required to interrogate and manipulate atomic transitions with long coherence times, which form the basis of optical atomic clocks[1,2]. Linewidth also directly impacts performance in optical sensing and signal generation applications such as laser gyroscopes[3,4], light detection and ranging (LIDAR) systems[5,6], spectroscopy[7], optical frequency synthesis[8], microwave photonics[9–13] and coherent optical communications[14,15]. In considering the future transfer of such high-coherence technologies to a mass-manufacturable form, semiconductor laser sources represent the most compelling choice. They are directly electrically pumped, wafer-scale manufacturable and capable of complex integration with other photonic devices. Indeed, their considerable advantages have made them into a kind of 'photonic engine' for nearly all modern-day optical source technology, including commercial bench-top laser sources. Nonetheless, mass-manufacturable semiconductor lasers, such as those used in communications systems, have linewidths ranging from 100 kHz to a few megahertz[14], which is many orders of magnitude too large for the above-mentioned applications.

A powerful method to narrow the linewidth of a laser is to apply optical feedback through an external reflector, for which the degree of noise suppression scales with the square of the quality (*Q*) factor of the reflector[16–22]. Ultra-high-*Q* microresonators are excellent candidates to achieve substantial linewidth narrowing and have been demonstrated across a wide range of materials as discrete[21,23] or integrated components[3,24–33]. To compare laser linewidths from different works, the short-term linewidth—indicated by the level of the high-offset-frequency white-noise floor—is a useful metric. Hereon, 'linewidth' refers to the short-term linewidth. Although sub-hertz linewidths have been realized in semiconductor lasers that are self-injection-locked to discrete crystalline microresonators[21], retaining ultra-high *Q* factor when moving to higher levels of integration is both of paramount importance and challenging. As a measure of the level of difficulty, current demonstrations of narrow-linewidth integrated lasers, despite many years of effort, feature linewidths of 40 Hz to 1 kHz, as limited by their *Q* factors[34–38].

In this work, we present critical advances in silicon nitride waveguides fabricated in a high-volume complementary metal–oxide–semiconductor (CMOS) foundry. We achieve a *Q* factor of over 260 million (M), which is high compared with the integrated resonators demonstrated thus far. By self-injection-locking a conventional semiconductor distributed-feedback (DFB) laser to these ultra-high-*Q* microresonators, we reduce the noise by five orders of magnitude, yielding a frequency noise of 0.2 Hz² Hz⁻¹ at high offset frequency, with a corresponding short-term linewidth of 1.2 Hz—a previously unattainable level for integrated lasers. Within the same configuration, a new regime of Kerr comb operation in microresonators is supported. Specifically, the comb demonstrates turnkey operation[38] as well as attaining coherent comb operation under conditions of normal dispersion, without any special dispersion engineering. The comb's line spacing is suitable for dense wavelength division multiplexed (DWDM) communications systems. Moreover, each comb line benefits from the exceptional frequency-noise performance of the disciplined pump, representing an important advance for DWDM source technology. The microwave phase noise performance of the comb is also comparable to that of existing commercial microwave oscillators. Overall, experiment and theory reveal an ultra-low-noise regime in integrated photonics.

Results

CMOS-ready ultra-high-*Q* microresonators. The resonators with ultra-high *Q* factor use high-aspect-ratio Si_3N_4 waveguides, as shown in Fig. 1a. The samples were fabricated in a high-volume CMOS foundry on 200-mm wafers (Fig. 1b) following the process of Bauters et al.[39], but we increased the thickness of the Si_3N_4 core from 40 nm to 100 nm. This thicker Si_3N_4 enabled a bending radius below 1 mm (Supplementary Information), allowing higher integration density than the centimetre-sized resonators demonstrated

[1]ECE Department, University of California Santa Barbara, Santa Barbara, CA, USA. [2]T. J. Watson Laboratory of Applied Physics, California Institute of Technology, Pasadena, CA, USA. [3]Anello Photonics, Santa Clara, CA, USA. [4]These authors contributed equally: Warren Jin, Qi-Fan Yang, Lin Chang, Boqiang Shen, Heming Wang. ✉e-mail: vahala@caltech.edu; bowers@ece.ucsb.edu

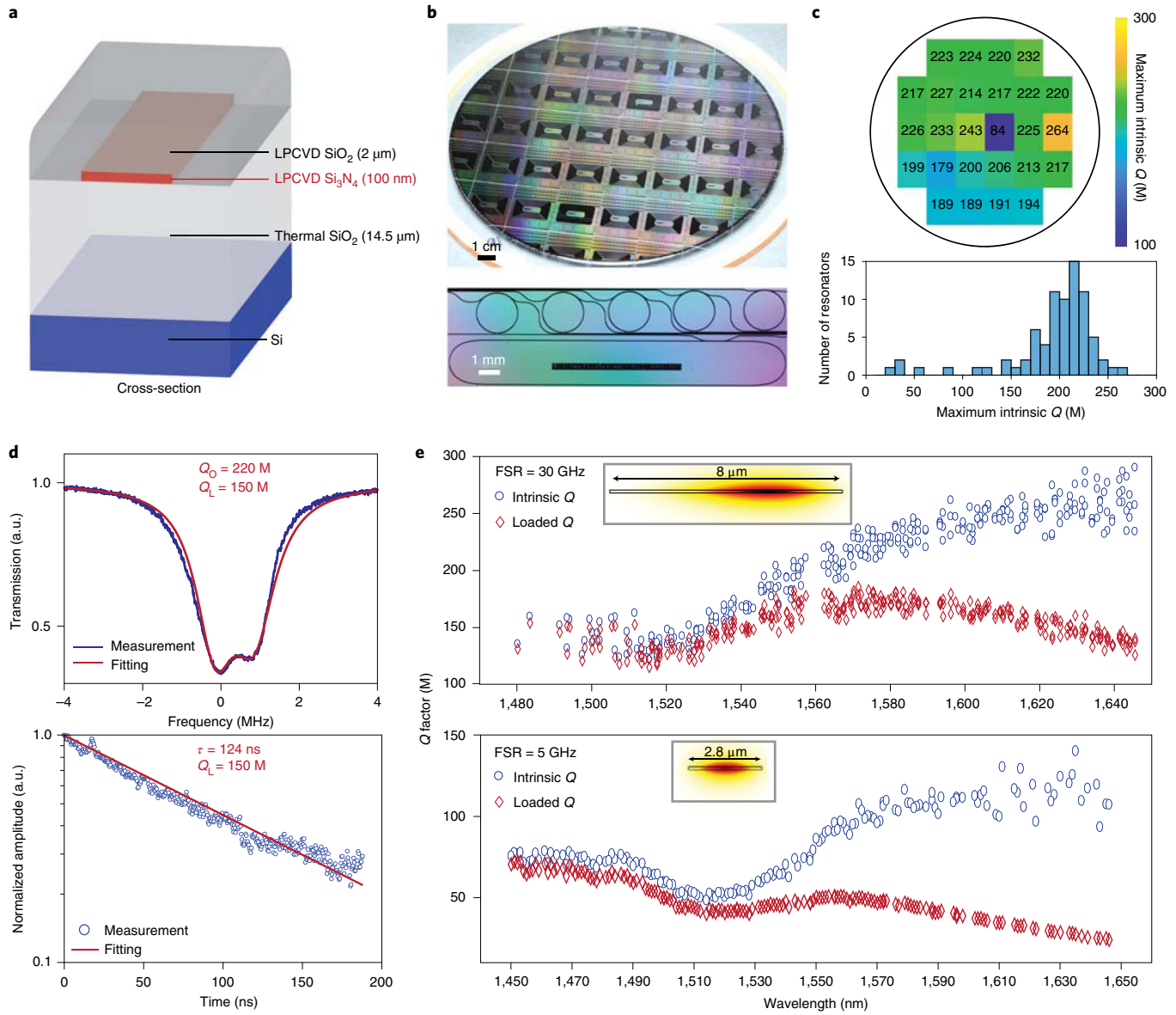

Fig. 1 | CMOS-ready ultra-high-Q Si_3N_4 microresonators. a, Cross-sectional diagram of the ultra-low-loss waveguide consisting of Si_3N_4 as the core material, silica as the cladding and silicon as the substrate (not to scale). **b**, Photograph of a CMOS-foundry-fabricated 200-mm-diameter wafer after dicing (top), and a top view showing the 30 GHz FSR Si_3N_4 ring resonators and a 5 GHz FSR racetrack resonator from a different reticle (bottom). **c**, The *Q* factors for each of three 30 GHZ FSR ring resonators on each of the 26 dies of the wafer shown in **b**, calculated as the average *Q* factor in the 1,620–1,650 nm range. The *Q* factors are shown as a wafer map of the highest *Q* factor on each die (top) and as a histogram of *Q* factors of the 78 resonators (bottom), demonstrating that ultra-high *Q* values are achieved across the wafer. **d**, Transmission spectrum (top) of a high-*Q* mode at 1,560 nm in a 30 GHz ring resonator. Interfacial and volumetric inhomogeneities induce Rayleigh scattering, causing resonances to appear as doublets due to coupling between counter-propagating modes. The intrinsic *Q* of 220 million (M) and loaded *Q* of 150 M are extracted by fitting the asymmetric mode doublet. The ring-down trace of the mode (bottom) shows a photon lifetime of 124 ns, corresponding to a loaded *Q* of 150 M. **e**, Measured intrinsic *Q* factors plotted versus wavelength in a 30 GHz ring resonator with 8-μm-wide Si_3N_4 core (top) and a 5 GHz racetrack resonator with 2.8-μm-wide Si_3N_4 core (bottom). Insets: simulated optical mode profiles.

previously[3,24,25]. Furthermore, a top cladding thickness of 2 μm was sufficient, obviating the need for complex chemical–mechanical polishing and bonding of additional thermal SiO_2 on top[24,39]. To minimize the residual hydrogen content of the deposited Si_3N_4 and SiO_2 films, we also used extended thermal treatment totalling over 20 h of annealing at 1,150 °C. Microresonators with three different free spectral ranges (FSRs) were fabricated. Those with FSR of 30 GHz were in a whispering-gallery-mode ring geometry, while single-mode racetrack resonators with FSRs of 5 and 10 GHz were fabricated to reduce the footprint (Fig. 1b).

The capability of CMOS-foundry fabrication to produce ultra-high *Q* factors at a wafer scale is exhibited in Fig. 1c, in which the intrinsic *Q* factors of 30 GHz FSR ring resonators measured throughout the wafer are observed to be clustered in the 170 M to 270 M range. The die map in Fig. 1c shows that an intrinsic *Q* factor in the vicinity of 200 M is observed on each die, with the exception

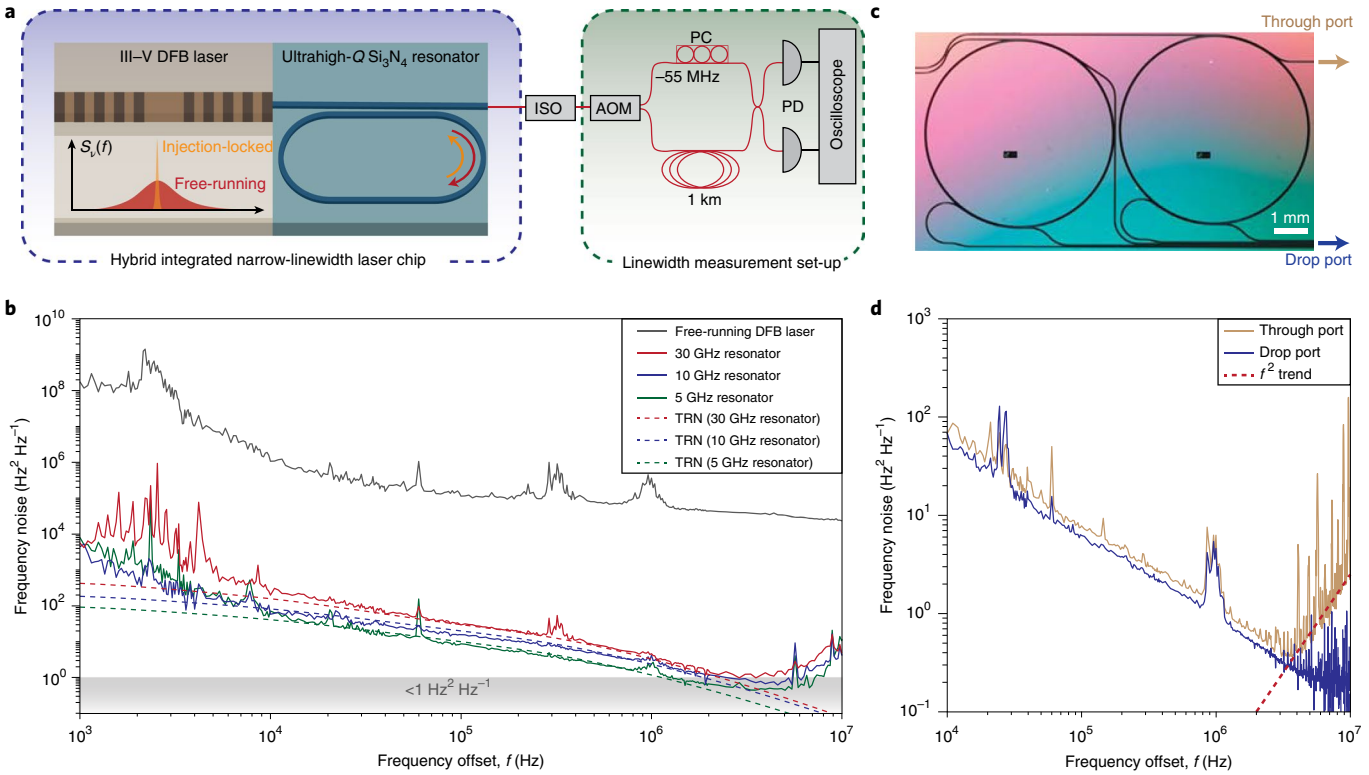

Fig. 2 | Hybrid integrated narrow-linewidth laser based on the ultra-high-*Q* Si_3N_4 microresonator. a, Schematic of the hybrid laser design (not to scale) and frequency-noise test set-up. The red (yellow) arrow denotes the forward (backscattered) light field. ISO, optical isolator; AOM, acousto-optic modulator; PC, polarization controller; PD, photodetector. **b**, Measurement of the single-sideband frequency noise of the free-running and self-injection-locked DFB laser. The minimum frequency-noise levels are 1.0, 0.8 and 0.5 $Hz^2 Hz^{-1}$ for resonators with 30 GHz, 10 GHz and 5 GHz FSRs, respectively. The dashed lines show the simulated thermorefractive noise (TRN) for the three resonators. **c**, Photograph of a 10.8 GHz FSR ring resonator fabricated with a drop port. **d**, A comparison of single-sideband frequency noise measured from the through port and drop port of the same device. The drop port enables the resonator itself to act as a low-pass filter, yielding a white-noise floor of 0.2 $Hz^2 Hz^{-1}$.

of a single die at the centre that was subject to handling error during fabrication. These *Q* factors were measured by performing transmission spectra scans using a tunable external cavity laser (calibrated by a separate interferometer) to extract the resonator linewidth and to infer the loaded, coupled and intrinsic optical *Q* factors. Cavity ring-down was also performed as a separate check of these *Q* measurements. Spectra were observed to occur in doublets on account of both the ultra-high *Q* and the presence of waveguide backscattering (Fig. 1d)[40]. By fitting the doublet line shape of the 30 GHz ring resonator, the intrinsic *Q* of 220 M and loaded *Q* of 150 M were extracted at 1,560 nm and were further confirmed by measuring the ring-down trace of the resonance, as shown in Fig. 1d. The spectral dependences of the *Q* factors in ring and racetrack resonators (Fig. 1e) provide insight into the origins of loss. A reduction in the value of *Q* around 1,510 nm is due to absorptive N–H bonds in the Si_3N_4 core. Beyond this wavelength, the intrinsic *Q* factor increases monotonically versus wavelength, probably limited by Rayleigh scattering. The highest *Q* factor is obtained using a 30 GHz FSR resonator (mean value of 260 M and standard deviation of 13.5 M over 34 modes) and is observed in the 1,630–1,650 nm wavelength range. The overall lower *Q* factor of the 5 GHz racetrack resonator suggests excess propagation loss in its single-mode waveguides. This is possibly caused by higher scattering loss from increased modal overlap with the waveguide side wall compared to the whispering-gallery mode waveguide.

Hertz-linewidth integrated laser. The hybrid integrated laser comprises a commercial DFB laser butt-coupled to the bus waveguide of the Si_3N_4 resonator chip (Fig. 2a). The laser chip, which is mounted on a thermoelectric cooler to avoid long-term drift, is able to deliver power up to 30 mW at 1,556 nm into the Si_3N_4 bus waveguide. Optical feedback is provided to the laser by backward Rayleigh scattering in the microresonator, which spontaneously aligns the laser frequency to the nearest resonator mode. As the phase accumulated in the feedback is critical to determining the stability of injection locking[22,38,41], we precisely control the feedback phase by adjusting the air gap between the chips. In the case of a rigidly co-packaged laser and resonator, feedback phase control may instead be achieved by the addition of a resistive heater to the waveguide linking the laser and resonator. The laser output is taken through the bus waveguide of the microresonator and directed to a self-heterodyne set-up for frequency-noise characterization. Two photodetectors and a cross-correlation technique are used to improve detection sensitivity[42] (Methods).

The frequency-noise spectra of the self-injection-locked laser system using the 30 GHz ring and the 10 GHz and 5 GHz racetrack resonators (respective intrinsic *Q* factors of 250 M, 56 M and 100 M) are compared in Fig. 2b. The ultra-high *Q* factors in principle enable the frequency noise of the free-running DFB laser to be suppressed by up to 80 dB (Methods). In practice, however, the noise suppression over a broad range of offset frequencies (10 kHz to 2 MHz) is limited to 50 dB by the presence of thermorefractive noise[43–45] in the microresonator. Consistent with theory, microresonators with larger mode volume (that is, smaller FSR) experience a lower thermorefractive fluctuation and exhibit reduced frequency noise (Fig. 2b). At low frequency offset (below 10 kHz), frequency noise is primarily limited by temperature drift and coupling stability between chips. This can be suppressed by improvements in device

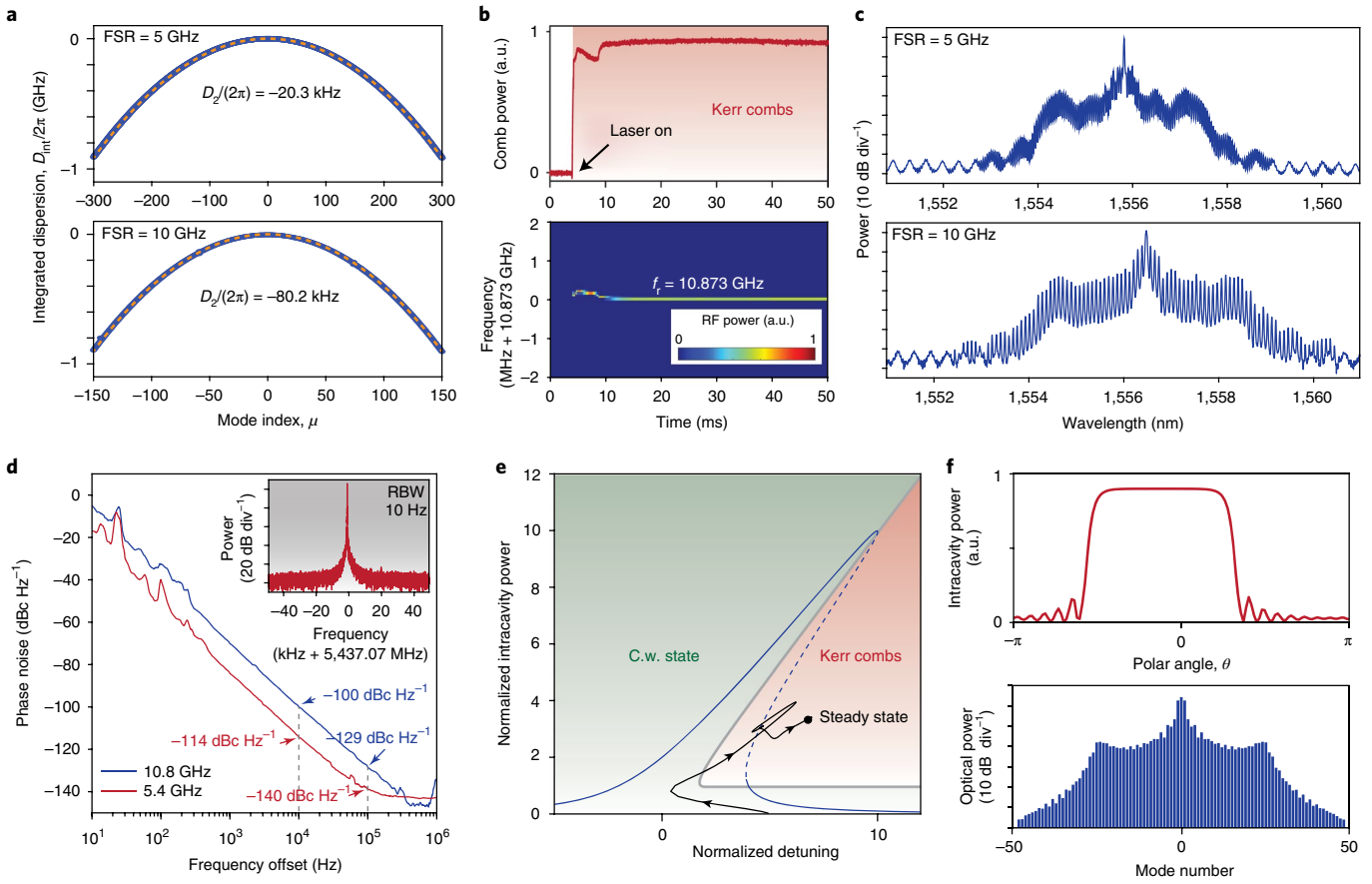

Fig. 3 | Formation of mode-locked Kerr combs. a, The measured mode family dispersion is normal. The plot shows the integrated dispersion, defined as $D_{int} = \omega_\mu - \omega_o - D_1\mu$ where ω_μ is the resonant frequency of a mode with index μ, ω_0 is the resonant frequency at $\mu = 0$, and D_1 is the FSR at $\mu = 0$. The wavelength of the central mode ($\mu = 0$) is around 1,550 nm. The dashed lines are parabolic fits ($D_{int} = D_2\mu^2/2$) with $D_2/2\pi$ equal to −20.3 kHz and −80.2 kHz corresponding to 5 GHz and 10 GHz FSRs, respectively. Note that $D_2 = -cD_1^2\beta_2/n_{eff}$, where β_2 is the group velocity dispersion, c is the speed of light and n_{eff} is the effective index of the mode. **b**, Experimental comb power (top) and detected comb repetition rate signal (bottom) with laser turn-on indicated at 5 ms. **c**, Measured optical spectra of mode-locked Kerr combs with 5 GHz (top) and 10 GHz (bottom) repetition rates. The background fringes are attributed to the DFB laser. **d**, Single-sideband phase noise of dark pulse repetition rates. Dark pulses with repetition rates of 10.8 GHz and 5.4 GHz are characterized. Inset: electrical beatnote showing the repetition rate of 5.4 GHz. **e**, Phase diagram of the microresonator pumped by an isolated laser. The backscattering is assumed weak enough to not cause mode splittings. The detuning is normalized to one-half of the microresonator linewidth, while the intracavity power is normalized to the parametric oscillation threshold. Green and red shaded areas indicate regimes corresponding to the continuous-wave (c.w.) state and Kerr combs. The blue curve is the c.w. intracavity power, and stable (unstable) branches are indicated by solid (dashed) lines. The simulated evolution of the unisolated laser is plotted as a solid black curve, which first evolves towards the middle unstable branch of the c.w. intracavity power curve and then converges to the comb steady state (average normalized power shown) as marked by the black dot. The initial condition is set within the self-injection-locking bandwidth[38], while the feedback phase is set to 0. **f**, Simulated intracavity field (top) and optical spectrum (bottom) of the unisolated laser steady state in **e**.

packaging. At high offset frequencies (above 5 MHz), frequency noise rises with the square of the offset frequency, as the maximum noise suppression bandwidth of injection locking is limited to the bandwidth of the resonator (Supplementary Information)[19,20]. Thus, a minimum frequency noise below 1 Hz^2 Hz^{-1} is observed at an offset frequency of ~5 MHz, where the contributions of rising laser noise and falling thermorefractive noise are approximately equal. To achieve an ultra-low white frequency noise floor at high offset frequencies, the laser output is taken from a resonator featuring a drop port[46] (Fig. 2c). The drop port provides low-pass filtering action and is studied further in the Supplementary Information. This configuration yields a white-noise floor of 0.2 Hz^2 Hz^{-1}, corresponding to a short-term linewidth of 1.2 Hz (Fig. 2d).

Mode-locked Kerr comb. The ultra-high Q of the microresonators enables strong resonant build-up of the circulating intensity, providing access to nonlinear optical phenomena at low input power levels[47]. As an example, optical frequency combs have been realized in continuously pumped high-Q optical microresonators due to the Kerr nonlinearity and are finding a wide range of applications[48]. To explore the nonlinear operating regime of the hybrid integrated laser in pursuit of highly coherent Kerr combs, we characterized the mode dispersion of racetrack resonators with 5 GHz and 10 GHz FSRs. Their mode families were measured to have normal dispersion across the telecommunication C-band (Fig. 3a). Furthermore, the dispersion curves exhibit no avoided mode crossings, consistent with the single-mode nature of the waveguides. As distinct from microresonators with anomalous dispersion wherein bright soliton pulses are readily generated, comb formation is forbidden in microresonators with normal dispersion, unless avoided mode crossings are introduced to alter the mode family dispersion to allow the formation of dark pulses[49]. Surprisingly, however, it was nonetheless

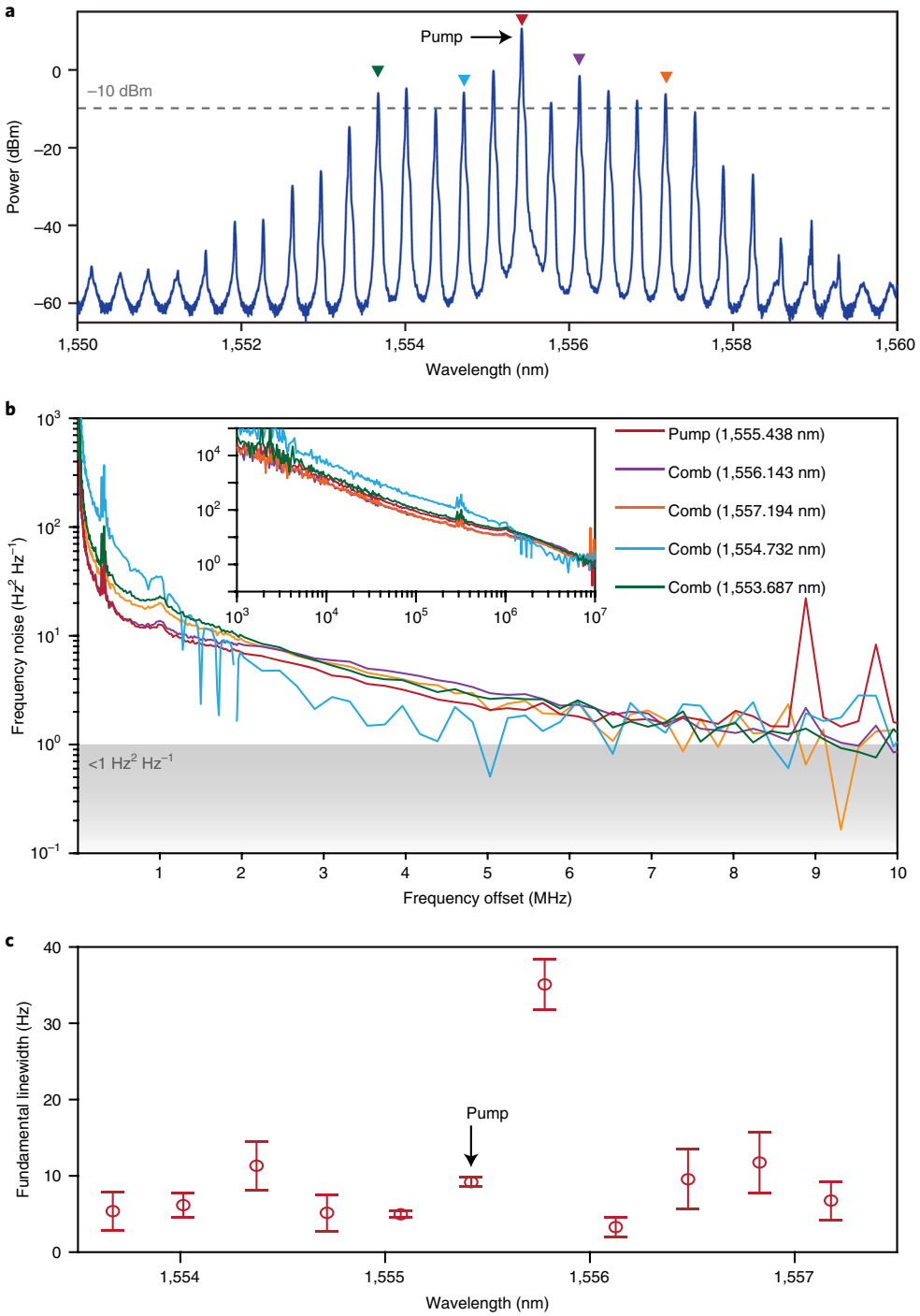

Fig. 4 | Coherence of integrated mode-locked Kerr combs. a, Optical spectrum of a mode-locked comb with a repetition rate of 43.2 GHz generated in a microresonator with 10.8 GHz FSR. **b**, Single-sideband optical frequency noise of the pump and comb lines as indicated in **a**, selected using a tunable fibre Bragg grating (FBG) filter. Inset: the same data but in log–log format. **c**, Wavelength dependence of the white-frequency-noise linewidth of the comb lines in **a**.

possible to readily form coherent combs in these devices without either of the aforementioned conditions being satisfied.

Indeed, deterministic turnkey comb formation was experimentally observed when the DFB laser was switched on to a preset driving current (Fig. 3b). A clean and stable comb beatnote is seen to be established 5 ms after turning on the laser, indicating that mode locking has been achieved (Fig. 3b). Plotted in Fig. 3c are optical spectra of the mode-locked Kerr combs in racetrack resonators with 5 GHz and 10 GHz FSRs, where the typical spectral shape of dark pulses is observed[48–51]. The stability of the mode locking is characterized by measurement of the comb beatnote phase noise (Fig. 3d). For Kerr combs with 10.8 (5.4) GHz FSR, the phase noise reaches −100 (−114) dBc Hz^{-1} at an offset frequency of 10 kHz and −129 (−140) dBc Hz^{-1} at 100 kHz. Note that, to suppress noise at high offset frequencies, the pump is excluded in photodetection using a fibre Bragg grating filter, as suggested by previous works[10].

This unexpected result is studied theoretically in the Supplementary Information. The results from that study are

Table 1 | Current integrated ultra-high-Q microresonators and narrow-linewidth lasers

Microresonators

Material	Cladding	Q (M)	FSR (GHz)	Finesse	Ref no.
Si_3N_4 (this work)	Oxide	260	30	42,600	
	Oxide	81	3.3	1,400	24
Si_3N_4 (low confinement)	Oxide	65	2.7	910	3
	Oxide	216	2.7	3,000	25
	Oxide	37	200	38,400	26
	Oxide	67	63	21,700	26
Si_3N_4 (high confinement)	Oxide	30	40	6,200	27
	Oxide	14	100	7,200	28
	Air	20	100	10,340	29
SiO_2	Air	205	15.2	15,800	30
Si	Oxide	22	5.4	630	31
$LiNbO_3$	Oxide	10	4	210	32
Phosphorus-doped silica	Doped oxide	31	1	170	33

Lasers

Operation principle	Configuration	Linewidth (Hz)	Ref no.
Self-injection locking (this work)	Hybrid III-V/Si_3N_4	1.2	
External cavity	Hybrid III-V/Si_3N_4	40	34
External cavity	Heterogeneous III-V/Si	140	35
External cavity	Heterogeneous III-V/Si_3N_4	4,000	36
External cavity	Monolithic III-V	50,000	58

Top: best integrated ultra-high-Q (>10 M) microresonators with integrated waveguides so far. Bottom: linewidths of best integrated narrow-linewidth lasers so far.

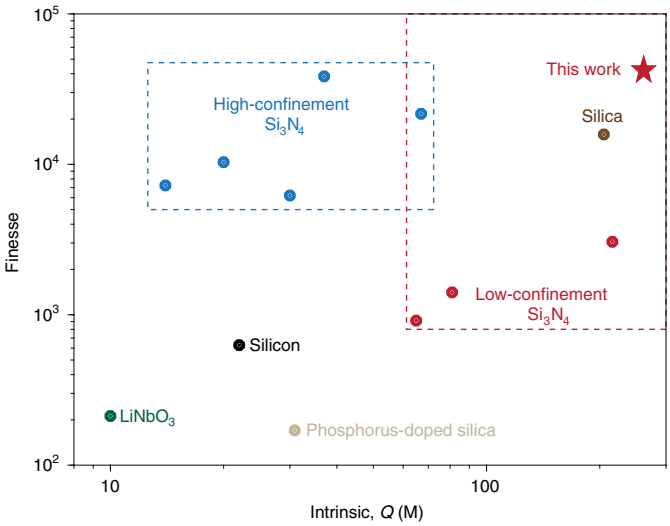

Fig. 5 | Comparison of finesse and intrinsic Q factors of state-of-the-art integrated microresonators. The present work is indicated by a red star.

summarized briefly here. A phase diagram of the microcomb system is presented in Fig. 3e, which separates the resonator operation into continuous-wave (c.w.) and Kerr comb regimes based on the viability of parametric oscillation[52]. The intracavity power exhibits a typical bi-stable behaviour as a function of cavity–pump frequency detuning when pumped by a laser with optical isolation[48]. In contrast, a recent study showed that the feedback from a nonlinear microresonator to a non-isolated laser creates an operating point for the compound laser–resonator system in the middle branch[38]. The operating point is induced through a combination of self- and cross-phase modulation, and is associated with turnkey operation of soliton combs operating under conditions of anomalous dispersion[38]. Here, we have validated through simulation that a similar operating point allows access to dark pulses (normal dispersion) without the requirement for extra dispersion engineering provided by avoided mode crossings. As has been shown previously for bright solitons, the phase of the feedback path plays a major role. Indeed, control of this phase through precision control of the coupling gap between the laser and resonator chips enabled suppression of comb formation for the frequency-noise measurements reported in Fig. 2b,d. The black curve in Fig. 3e shows the dynamics of the compound laser–resonator system when initialized at a point that is within the locking bandwidth of the system. It first evolves towards the operating point located on the middle branch of the c.w. power bi-stability curve, where comb formation can be initiated, and then converges to a steady Kerr comb state (average normalized power shown). The spectral and temporal profiles of the steady-state solutions show that flat-top pulses are formed in the microresonator with normal dispersion (Fig. 3f). Although the possible presence of dark pulse formation in microresonators pumped by a self-injection-locked laser has been previously observed[50,51,53], the theory of the mutually coupled system has only recently been clarified (Supplementary Information)[38,54,55].

The combs generated in these devices exhibit several important properties. Figure 4a presents the spectrum of a comb with a repetition rate of 43.2 GHz. Curiously, this spectrum was generated in a microresonator with a 10.8 GHz FSR. The appearance of rates that are different from the FSR rate has been observed for dark pulses[49]. This line spacing is compatible with DWDM channel spacings and ten of the comb teeth feature an on-chip optical power of over −10 dBm. This is a per-channel power that is readily usable in DWDM communication systems[56]. However, most importantly, the white-frequency-noise-level floor for each of these optical lines (Fig. 4b) is measured to be on the order of 1 $Hz^2 Hz^{-1}$. We note that the frequency noise levels of the comb lines do not rise at higher offset frequency, in contrast to the frequency noise of the laser source shown in Fig. 2b. The corresponding linewidths of the comb teeth are plotted in Fig. 4c. One of the lines exhibits a degraded linewidth of ~30 Hz, which is suspected to be due to its coincidence with a sub-lasing-threshold side mode of the DFB laser. Notably, certain comb teeth are quieter than the pump due to the filtering of pump noise by the ultra-high-Q modes. These results represent a two orders of magnitude improvement over previously demonstrated integrated microcombs[37,38,53,57].

Performance comparison. Among devices with an integrated waveguide coupler and resonator, a few platforms have emerged that are able to provide ultra-high Q values ($Q > 10$ M). In silica ridge resonators, a Q factor of 205 M has been demonstrated[30], while in low-confinement silicon nitride, a Q factor of 216 M has been demonstrated[25]. However, these platforms pose challenges to photonic integration at large scale and high density, for example, with the use of suspended structures[30] or the requirement for centimetre-level bending radius[25]. Although these limitations are not present in high-confinement silicon nitride resonators, the highest demonstrated Q factor is lower, at 67 M (ref. [26]). In Table 1, we list key figures of merit for integrated microresonators with ultra-high Q

factors. In addition to their high Q factors, because of their compact footprints the current resonators stand out among ultra-high-Q resonators for having high finesse values as well. Figure 5 provides a comparison as a plot of the Q and finesse of the current work and state-of-the-art devices.

Table 1 also compares the current hybrid integrated laser linewidth to state-of-the-art results. The linewidth of monolithic III–V lasers is generally limited to the 100 kHz to 1 MHz range by passive waveguide losses well above 1 dB cm^{-1}, with the best demonstrated linewidth being below 100 kHz (ref. [58]). Phase and amplitude noise scale according to the square of cavity losses[20,22]. Thus, hybrid integration, where the active III–V and passive photonic chips are assembled post-fabrication, and heterogeneous integration[59], where III–V material is directly bonded to the passive chip during fabrication, have emerged as the primary technologies to create narrow-linewidth integrated lasers. As shown in Table 1, hybrid and heterogeneous integration can produce linewidths well below 1 kHz. In this work, high-offset frequency noise is suppressed to a white noise floor of 0.2 Hz^2 Hz^{-1} or, equivalently, a short-term linewidth of 1.2 Hz, which is more than an order of magnitude improvement over the best results so far[34].

Discussion

As single-frequency or mode-locked lasers, these hybrid integrated devices are readily applicable to many coherent optical systems. For example, while laboratory communication experiments pursuing spectral efficiency approaching 20 bit s^{-1} Hz^{-1} rely on high-performance single-frequency fibre lasers[15], narrow-linewidth integrated photonic comb lasers could accelerate the adoption of similar schemes in practical data-centre and metro links[37,38,56,57,60,61]. Microwave photonics[9–13], atomic clocks[1,2] and quantum information[62] will also benefit greatly from the reduced size, weight, power and cost provided by the combination of ultra-high Q and photonic integration.

Many improvements beyond the results presented here are feasible. We infer a propagation loss of 0.1 dB m^{-1}, but a lower loss of 0.045 dB m^{-1} is feasible in thinner cores[39], suggesting that the limits of Q for this platform have not been fully explored. Spiral resonators with increased modal volume can suppress low-offset frequency noise induced by thermodynamic fluctuations[63]. Finally, heterogeneous integration of III–V lasers and ultra-high-Q microresonators may eventually unite the device onto a single chip[35,36,59], leading to scalable production with high yield using foundry-based technologies.

Note added in proof: During the review of our manuscript, another ultra-high-Q silicon-chip-based resonator was reported[64].

Online content

Any methods, additional references, Nature Research reporting summaries, source data, extended data, supplementary information, acknowledgements, peer review information; details of author contributions and competing interests; and statements of data and code availability are available at https://doi.org/10.1038/s41566-021-00761-7.

Received: 6 July 2020; Accepted: 7 January 2021;
Published online: 11 February 2021

References

1. Ludlow, A. D., Boyd, M. M., Ye, J., Peik, E. & Schmidt, P. O. Optical atomic clocks. *Rev. Mod. Phys.* **87**, 637–701 (2015).
2. Newman, Z. L. et al. Architecture for the photonic integration of an optical atomic clock. *Optica* **6**, 680–685 (2019).
3. Gundavarapu, S. et al. Sub-hertz fundamental linewidth photonic integrated brillouin laser. *Nat. Photon.* **13**, 60–67 (2019).
4. Lai, Y.-H. et al. Earth rotation measured by a chip-scale ring laser gyroscope. *Nat. Photon.* **14**, 345–349 (2020).
5. Trocha, P. et al. Ultrafast optical ranging using microresonator soliton frequency combs. *Science* **359**, 887–891 (2018).
6. Suh, M.-G. & Vahala, K. J. Soliton microcomb range measurement. *Science* **359**, 884–887 (2018).
7. Suh, M.-G., Yang, Q.-F., Yang, K. Y., Yi, X. & Vahala, K. J. Microresonator soliton dual-comb spectroscopy. *Science* **354**, 600–603 (2016).
8. Spencer, D. T. et al. An optical-frequency synthesizer using integrated photonics. *Nature* **557**, 81–85 (2018).
9. Li, J., Lee, H. & Vahala, K. J. Microwave synthesizer using an on-chip Brillouin oscillator. *Nat. Commun.* **4**, 2097 (2013).
10. Liang, W. et al. High spectral purity Kerr frequency comb radio frequency photonic oscillator. *Nat. Commun.* **6**, 7957 (2015).
11. Hao, T. et al. Toward monolithic integration of OEOs: from systems to chips. *J. Lightwave Technol.* **36**, 4565–4582 (2018).
12. Marpaung, D., Yao, J. & Capmany, J. Integrated microwave photonics. *Nat. Photon.* **13**, 80–90 (2019).
13. Liu, J. et al. Photonic microwave generation in the X- and K-band using integrated soliton microcombs.*Nat. Photon* **14**, 486–491 (2020).
14. Kikuchi, K. Fundamentals of coherent optical fiber communications. *J. Lightwave Technol.* **34**, 157–179 (2015).
15. Olsson, S. L. et al. Probabilistically shaped PDM 4096-QAM transmission over up to 200 km of fiber using standard intradyne detection. *Opt. Express* **26**, 4522–4530 (2018).
16. Dahmani, B., Hollberg, L. & Drullinger, R. Frequency stabilization of semiconductor lasers by resonant optical feedback. *Opt. Lett.* **12**, 876–878 (1987).
17. Hollberg, L. & Ohtsu, M. Modulatable narrow-linewidth semiconductor lasers. *Appl. Phys. Lett.* **53**, 944–946 (1988).
18. Hemmerich, A., McIntyre, D., Schropp, D.Jr, Meschede, D. & Hänsch, T. Optically stabilized narrow linewidth semiconductor laser for high resolution spectroscopy. *Opt. Commun.* **75**, 118–122 (1990).
19. Li, H. & Abraham, N. Analysis of the noise spectra of a laser diode with optical feedback from a high-finesse resonator. *IEEE J. Quantum Electron.* **25**, 1782–1793 (1989).
20. Hjelme, D. R., Mickelson, A. R. & Beausoleil, R. G. Semiconductor laser stabilization by external optical feedback. *IEEE J. Quantum Electron.* **27**, 352–372 (1991).
21. Liang, W. et al. Ultralow noise miniature external cavity semiconductor laser. *Nat. Commun.* **6**, 7371 (2015).
22. Kondratiev, N. et al. Self-injection locking of a laser diode to a high-Q WGM microresonator. *Opt. Express* **25**, 28167–28178 (2017).
23. Lee, H. et al. Chemically etched ultrahigh-Q wedge-resonator on a silicon chip. *Nat. Photon.* **6**, 369–373 (2012).
24. Spencer, D. T., Bauters, J. F., Heck, M. J. & Bowers, J. E. Integrated waveguide coupled Si_3N_4 resonators in the ultrahigh-Q regime. *Optica* **1**, 153–157 (2014).
25. Puckett, M. W. et al. Silicon nitride ring resonators with 0.123 dB/m loss and Q-factors of 216 million for nonlinear optical applications. In *Proc. 2019 Conference on Lasers and Electro-Optics Europe & European Quantum Electronics Conference* (*CLEO/Europe-EQEC*) ce_11_3 (OSA, 2019).
26. Ji, X. et al. Ultra-low-loss on-chip resonators with sub-milliwatt parametric oscillation threshold. *Optica* **4**, 619–624 (2017).
27. Liu, J. et al. High-yield wafer-scale fabrication of ultralow-loss, dispersion-engineered silicon nitride photonic circuits. Preprint at https://arxiv.org/abs/2005.13949 (2020).
28. Ye, Z., Twayana, K., Andrekson, P. A. & Torres-Company, V. High-Q Si_3N_4 microresonators based on a subtractive processing for Kerr nonlinear optics. *Opt. Express* **27**, 35719–35727 (2019).
29. Li, Q. et al. Vertical integration of high-Q silicon nitride microresonators into silicon-on-insulator platform. *Opt. Express* **21**, 18236–18248 (2013).
30. Yang, K. Y. et al. Bridging ultrahigh-Q devices and photonic circuits. *Nat. Photon.* **12**, 297–302 (2018).
31. Biberman, A., Shaw, M. J., Timurdogan, E., Wright, J. B. & Watts, M. R. Ultralow-loss silicon ring resonators. *Opt. Lett.* **37**, 4236–4238 (2012).
32. Zhang, M., Wang, C., Cheng, R., Shams-Ansari, A. & Lončar, M. Monolithic ultra-high-Q lithium niobate microring resonator. *Optica* **4**, 1536–1537 (2017).
33. Adar, R., Serbin, M. & Mizrahi, V. Less than 1 dB per meter propagation loss of silica waveguides measured using a ring resonator. *J. Lightwave Technol.* **12**, 1369–1372 (1994).
34. Fan, Y. et al. Hybrid integrated InP-Si_3N_4 diode laser with a 40-Hz intrinsic linewidth. *Opt. Express* **28**, 21713–21728 (2020).
35. Tran, M. A., Huang, D. & Bowers, J. E. Tutorial on narrow linewidth tunable semiconductor lasers using Si/III–V heterogeneous integration. *APL Photonics* **4**, 111101 (2019).
36. Xiang, C. et al. Narrow-linewidth III–V/Si/Si_3N_4 laser using multilayer heterogeneous integration. *Optica* **7**, 20–21 (2020).
37. Raja, A. S. et al. Electrically pumped photonic integrated soliton microcomb. *Nat. Commun.* **10**, 680 (2019).
38. Shen, B. et al. Integrated turnkey soliton microcombs. *Nature* **582**, 365–369 (2020).

39. Bauters, J. F. et al. Planar waveguides with less than 0.1 db/m propagation loss fabricated with wafer bonding. *Opt. Express* **19**, 24090–24101 (2011).
40. Kippenberg, T. J., Spillane, S. M. & Vahala, K. J. Modal coupling in traveling-wave resonators. *Opt. Lett.* **27**, 1669–1671 (2002).
41. Savchenkov, A., Williams, S. & Matsko, A. On stiffness of optical self-injection locking. *Photonics* **5**, 43 (2018).
42. Wang, H., Wu, L., Yuan, Z. & Vahala, K. Towards milli-hertz laser frequency noise on a chip. Preprint at https://arxiv.org/abs/2010.09248 (2020).
43. Kondratiev, N. & Gorodetsky, M. Thermorefractive noise in whispering gallery mode microresonators: analytical results and numerical simulation. *Phys. Lett. A* **382**, 2265–2268 (2018).
44. Huang, G. et al. Thermorefractive noise in silicon-nitride microresonators. *Phys. Rev. A* **99**, 061801 (2019).
45. Lim, J. et al. Chasing the thermodynamical noise limit in whispering-gallery-mode resonators for ultrastable laser frequency stabilization. *Nat. Commun.* **8**, 8 (2017).
46. Wang, P.-H. et al. Drop-port study of microresonator frequency combs: power transfer, spectra and time-domain characterization. *Opt. Express* **21**, 22441–22452 (2013).
47. Vahala, K. J. Optical microcavities. *Nature* **424**, 839–846 (2003).
48. Kippenberg, T. J., Gaeta, A. L., Lipson, M. & Gorodetsky, M. L. Dissipative Kerr solitons in optical microresonators. *Science* **361**, aan8083 (2018).
49. Xue, X. et al. Mode-locked dark pulse Kerr combs in normal-dispersion microresonators. *Nat. Photon.* **9**, 594–600 (2015).
50. Liang, W. et al. Generation of a coherent near-infrared Kerr frequency comb in a monolithic microresonator with normal GVD. *Opt. Lett.* **39**, 2920–2923 (2014).
51. Lobanov, V., Lihachev, G., Kippenberg, T. & Gorodetsky, M. Frequency combs and platicons in optical microresonators with normal GVD. *Opt. Express* **23**, 7713–7721 (2015).
52. Godey, C., Balakireva, I. V., Coillet, A. & Chembo, Y. K. Stability analysis of the spatiotemporal Lugiato–Lefever model for Kerr optical frequency combs in the anomalous and normal dispersion regimes. *Phys. Rev. A* **89**, 063814 (2014).
53. Lihachev, G. V. et al. Laser self-injection locked frequency combs in a normal GVD integrated microresonator. In *Proc. Conference on Lasers and Electro-Optics*, *OSA Technical Digest* STh1O.3 (OSA, 2020).
54. Kondratiev, N. M. & Lobanov, V. E. Modulational instability and frequency combs in whispering-gallery-mode microresonators with backscattering. *Phys. Rev. A* **101**, 013816 (2020).
55. Kondratiev, N. M., Voloshin, A. S., Lobanov, V. E. & Bilenko, I. A. Numerical modelling of WGM microresonator Kerr frequency combs in self-injection locking regime. In *Proc. Nonlinear Optics and its Applications 2020*, Vol. 11358, 113580O (International Society for Optics and Photonics, 2020).
56. Fülöp, A. et al. High-order coherent communications using mode-locked dark-pulse Kerr combs from microresonators. *Nat. Commun.* **9**, 1598 (2018).
57. Stern, B., Ji, X., Okawachi, Y., Gaeta, A. L. & Lipson, M. Battery-operated integrated frequency comb generator. *Nature* **562**, 401–405 (2018).
58. Larson, M. et al. Narrow linewidth sampled-grating distributed Bragg reflector laser with enhanced side-mode suppression. In *Proc. 2015 Optical Fiber Communications Conference and Exhibition* (*OFC*) 1–3 (IEEE, 2015).
59. Komljenovic, T. et al. Heterogeneous silicon photonic integrated circuits. *J. Lightwave Technol.* **34**, 20–35 (2016).
60. Marin-Palomo, P. et al. Microresonator-based solitons for massively parallel coherent optical communications. *Nature* **546**, 274–279 (2017).
61. Corcoran, B. et al. Ultra-dense optical data transmission over standard fibre with a single chip source. *Nat. Commun.* **11**, 2568 (2020).
62. Tanzilli, S. et al. On the genesis and evolution of integrated quantum optics. *Laser Photon. Rev.* **6**, 115–143 (2012).
63. Lee, H. et al. Spiral resonators for on-chip laser frequency stabilization. *Nat. Commun.* **4**, 2468 (2013).
64. Puckett, M. W. et al. 422 million Q planar integrated all-waveguide resonator with a 3.4 billion absorption-limited Q and sub-MHz linewidth. Preprint at https://arxiv.org/abs/2009.07428 (2020).

Methods

Experimental details. Q factors were obtained by frequency down-scanning an external-cavity diode laser across a mode, with the frequency calibrated using a Mach–Zehnder interferometer (MZI). Measured transmission spectra at various wavelengths are shown in the Supplementary Information. Similarly, the mode family dispersion was extracted from the broadband transmission spectrum of the resonator, with calibration also provided by the MZI.

The laser switch-on test was performed by rapidly modulating its driving current with square wave functions. Real-time evolution of the comb repetition rate was obtained by down-mixing the photodetected beatnote with a local microwave oscillator. The trace, which was recorded using a high-speed oscilloscope, was Fourier-transformed to give the spectrograph. Multiple turnkey tests with 100% success rate are shown in the Supplementary Information). The phase noise of the comb repetition rates was characterized using a Rohde & Schwarz phase noise analyser.

Laser linewidth measurement. Noise in the photodetection (for example, shot noise, thermal noise and dark current) limits the sensitivity of the self-heterodyne method, especially at high offset frequencies. To overcome this limitation, we used two photodetectors to measure the self-heterodyne signals simultaneously. Detailed analysis on the performance of this set-up is provided elsewhere[42]. The instantaneous frequency was extracted using Hilbert transformation, and the cross-correlation $C_\nu(f)$ is given by

$$\begin{aligned} C_\nu(f) &= 2\left(1-(1-\tau_0\mathrm{BW})^+\cos(2\pi f\tau_0)\right)S_\nu(f) \\ &- \tfrac{1}{2}\left(1+(1-\tau_0\mathrm{BW})^+\cos(2\pi f\tau_0)\right) \\ &\times f^2(S_I(f_c+f)+S_I(f_c-f)) \end{aligned} \quad (1)$$

where $S_\nu(f)$ and $S_I(f)$ are the single-sideband power spectral densities of the frequency and relative intensity noise (RIN) of the laser, τ_0 is the delay between the two arms, f_c is a carrier offset frequency introduced using an acousto-optic modulator, and $x^+ = \max(0, x)$ is the ramp function. The resolution bandwidth (BW) of the cross-correlator is set to 20 kHz so that $\tau_0\mathrm{BW} \ll 1$. To reduce the contribution of the RIN as well as enhance the detection sensitivity of the frequency noise, at high offset frequencies ($f > 2$ MHz) we only select the data where $\cos(2\pi f\tau_0) \approx -1$. The enhancement of sensitivity equals $\sqrt{\mathrm{BW}\times T}$, where T is the recording time. In this measurement, T is set to 200 ms, corresponding to an 18 dB enhancement of sensitivity.

Thermorefractive noise. Constant heat exchange between the microresonator and its ambient results in thermodynamic fluctuations, which could induce changes in the refractive index through the thermo-optic effect, giving rise to thermorefractive noise (TRN) in the resonant frequencies[43,44]. The variance of the TRN is given by

$$\langle\delta\omega_c^2\rangle = \frac{n_T^2\omega_c^2}{n_{\mathrm{eff}}^2}\frac{k_B T^2}{\rho C V} \quad (2)$$

where n_T is the thermo-optic coefficient, ω_c is the resonant frequency, n_{eff} is the effective index of the mode, k_B is Boltzmann's constant, T is the temperature of the heat bath, ρ is the density, C is the specific heat and V is the volume. Owing to their larger mode volumes, the low-confinement resonators in this work feature notably smaller TRN than high-confinement resonators[44]. The spectral density of the TRN is computed using a finite element method based on the fluctuation–dissipation theorem[22], as plotted in Fig. 2b in the main text.

Noise reduction factor. The amount of noise reduction in a self-injection-locked laser depends on the spectral response and power of the backscattered field, which is derived in the Supplementary Information based on a complete theory involving both laser and microresonator dynamics[22]. We introduce a coupling β between the clockwise and counterclockwise field in the microresonator, which is normalized to one-half of the cavity linewidth. In the case of weak backscattering ($\beta \ll 1$)—that is, the mode remains as a singlet—the laser frequency noise can be reduced by the noise reduction factor (NRF):

$$\mathrm{NRF} \approx 64(1+\alpha^2)T^2\eta^2|\beta|^2\frac{Q_R^2}{Q_d^2} \quad (3)$$

where Q_R and Q_d are the Q value for the microresonator and the laser diode, respectively, and $\eta = Q_R/Q_e$ is the microresonator loading factor, with Q_e being the coupling Q between the bus waveguide and the resonator. T denotes the power insertion loss between the facets of the laser and the bus waveguide, while α is the amplitude–phase coupling coefficient of the laser. In the presence of a strong backscattered field ($\beta \gg 1$)—that is, the mode splits into doublets—the NRF is saturated as

$$\mathrm{NRF} \approx 4(1+\alpha^2)T^2\eta^2\frac{Q_R^2}{Q_d^2} \quad (4)$$

which is independent of the backscattering coefficient. Typical values of these parameters in our systems are $\alpha = 2.5$, $T = -6$ dB, $\eta = 0.5$ and $Q_d = 10^4$. For the mode featuring a loaded Q of 50 M and split resonances, the maximum estimated NRF is ~70 dB, which is 20 dB higher than the noise suppression achieved in the experiment. Measurements of noise for c.w. laser action were made under conditions of feedback phase offset so as to avoid comb formation. This condition could also contribute to a reduced NRF and is under investigation.

Phase diagram. The phase diagram presented in Fig. 3e is a powerful tool to interpret how self-injection locking can deterministically lead to mode-locked Kerr comb formation. Assuming a homogeneous intracavity field, the parametric gain of the $\pm l_{\mathrm{th}}$ modes relative to the pump is given by[52]

$$\Gamma(\pm l) = \mathrm{Re}\left\{-1+\sqrt{\rho^2-\left(\Delta-2\rho+d_2 l^2\right)^2}\right\} \quad (5)$$

where ρ^2 is the intracavity power normalized to the parametric oscillation threshold[48], $\Delta = 2\delta\omega/\kappa$ is the normalized detuning (κ is the modal linewidth and $\delta\omega$ is the pump–cavity detuning) and $d_2 = D_2/\kappa$ is the normalized dispersion. To initiate parametric oscillation, $\Gamma(\pm l) > 0$ is required. At the minimal value of $l^2 = 1$, the regime corresponding to a Kerr comb is given by

$$\Delta > 2\rho - d_2 - \sqrt{\rho^2 - 1} \quad (6)$$

Data availability

All data generated or analysed during this study are available within the paper and its Supplementary Information. Further source data will be made available on reasonable request.

Code availability

The analysis codes will be made available on reasonable request.

Acknowledgements

We acknowledge support from the Defense Advanced Research Projects Agency (DARPA) under the DODOS (HR0011-15-C-055) and APHI (FA9453-19-C-0029) programmes and Anello Photonics.

Author contributions

The experiments were conceived by W.J., Q.-F.Y., L.C., B.S. and H.W. The devices were designed by W.J. and A.F. Measurements were performed by W.J., Q.-F.Y., L.C., B.S. and H.W., with assistance from M.A.L., L.W. and M.G. Analysis of the results was conducted by W.J., Q.-F.Y. and H.W. The project was coordinated by Q.-F.Y. and L.C. under the supervision of J.E.B., K.J.V. and M.P. All authors participated in writing the manuscript.

Competing interests

The authors declare no competing interests.

Additional information

Supplementary information The online version contains supplementary material available at https://doi.org/10.1038/s41566-021-00761-7.

Correspondence and requests for materials should be addressed to K.J.V. or J.E.B.

Peer review information *Nature Photonics* thanks Andrey Matsko, Michael Watts and the other, anonymous, reviewer(s) for their contribution to the peer review of this work.

Reprints and permissions information is available at www.nature.com/reprints.